COGEAR

MODULE 3:

Preparation of soil slope failure related to seismic shaking

Del. No.: 3b.3.7

Authors: Chao L., Dupray F., and Laloui, L.

Laboratory of Soil Mechanics, EPFL

July 12, 2012

ENAC - Faculté Environnement naturel, architectural et construit
LMS - Laboratoire de mécanique des sols

EPFL - LMS
Station 18
CH - 1015 Lausanne

Tél.: +41 (0)21 693 23 15
Fax: +41 (0)21 693 41 53
Web: http://lms.epfl.ch

ÉCOLE POLYTECHNIQUE
FÉDÉRALE DE LAUSANNE

Competence Center Environment and Sustainability

COGEAR: COupled seismogenic GEohazards in Alpine Regions

MODULE 3 – Deliverable 3b.3.7

Preparation of soil slope failure related to seismic shaking

2D sensitivity analysis of a case study in Grächen

Authors: L. Chao, Dr F. Dupray, Prof. L. Laloui

Table of contents

Introduction

Local soil conditions have the potential to affect the intensity of damages created by a seism at a given site. These conditions encompass two main aspects, the geometry of the site, also known as the site effect, and the dynamic behaviour of the soil layers. The first aspect is studied especially in the case of bottom of valleys, and that is the case in COGEAR project module 3a. It is less well-known for other situations such as a definite zone of soil on a mountain slope: this aspect is treated in this report. The last aspect, dynamic behaviour of soil layers, or lithological site effect, is the focus point of deliverable 3b.3.6.

Swiss Seismological Service underlined in the report *Seismic hazard assessment of Switzerland* (Giardini *et al.* 2004) that the region of Valais will continue being a very seismically active zone for example, the village of Grächen. In addition, the site of the village lies on a deep-seated rock movement, and is close to known trajectories of rock avalanches. The evaluation of risks for this particular village is therefore representative of a worst case situation at the scale of Switzerland. The village lies on between 30 and 80 m of soil layers, while rock is apparent above and below the village.

However, it is hard to define the effect of individual factors on slope instability because of their mutual interactions. In addition, dynamic effects of earthquake will significantly increase complexity of slope stability problem. As a consequence, it is needed to understand the dynamic behaviour of soil during a seism in conditions close to the reality. The objective of this specific report is to complete the conclusions of report 3b.3.6 in terms of 2D effects and sensitivity to hydraulic and mechanical characteristics.

This work is divided into three parts. The overview of the topic of landslides and seisms in Valais is addressed in report 3b.3.6 and is not repeated here, but details on the geology of the site are presented. The theoretical formulations that are used in this study are then described with emphasis put on different aspects of soil dynamics concerning hydro-mechanical coupling and boundary conditions. The third part focuses on the numerical simulation that is used to draw conclusions for the site and as a case study. This report is concluded by summarization of the whole studies linked to seisms and soils in the site of Grächen.

1 Geology of the Grächen site

The mountainous area around the village of Grächen lies on a gneiss substratum. A large scale deep-seated rockslide of Randa Augengneiss occurred in geological times, and the area is still subject to movements of this deep-seated slide (see Del. 3b.3.1). This formation has been covered by more recent moraine deposits as well as some alluvial deposits locally.

In historic times, the area has also seen smaller scale geological events: debris flow and rock fall have been observed in the last two centuries, as well as small superficial landslides in the steeper area of the village. The results of these phenomena are still visible today. To the south of the village, the cone of a rock fall caused by a seism in 1855 is visible. Close to the village, under the church, small landslides are also visible: the probable cause for this is the presence of a diverted small canal on top of the hill that creates a hydraulic head in the area.

It should be noted that the deep seated rock slide is still active, although on a small scale. Details are available in COGEAR Del. 3b.3.1.

The geology cross section shown in Figure 2 is used for the 2D modelling. Its position is indicated in Figure 1 by a red line. In general, this cross section indicates that the village of Grächen is located on a 40 meters thick layer of soil stratum. More precise characterization of this soil stratum is available in Del. 3b.3.6. The large scale deep seated rock slide of Randa Augengneiss forms the substratum. Further up the village, the older strata are covered by recent alluvial deposits and there is a cone from a debris flow that stopped above the village. Our main interest focuses only on the village of Grächen because upper and lower parts of the village are mostly rock-covered. This aspect is treated in another part of the COGEAR project.

Figure 1: Location of the boreholes and geology of cross section

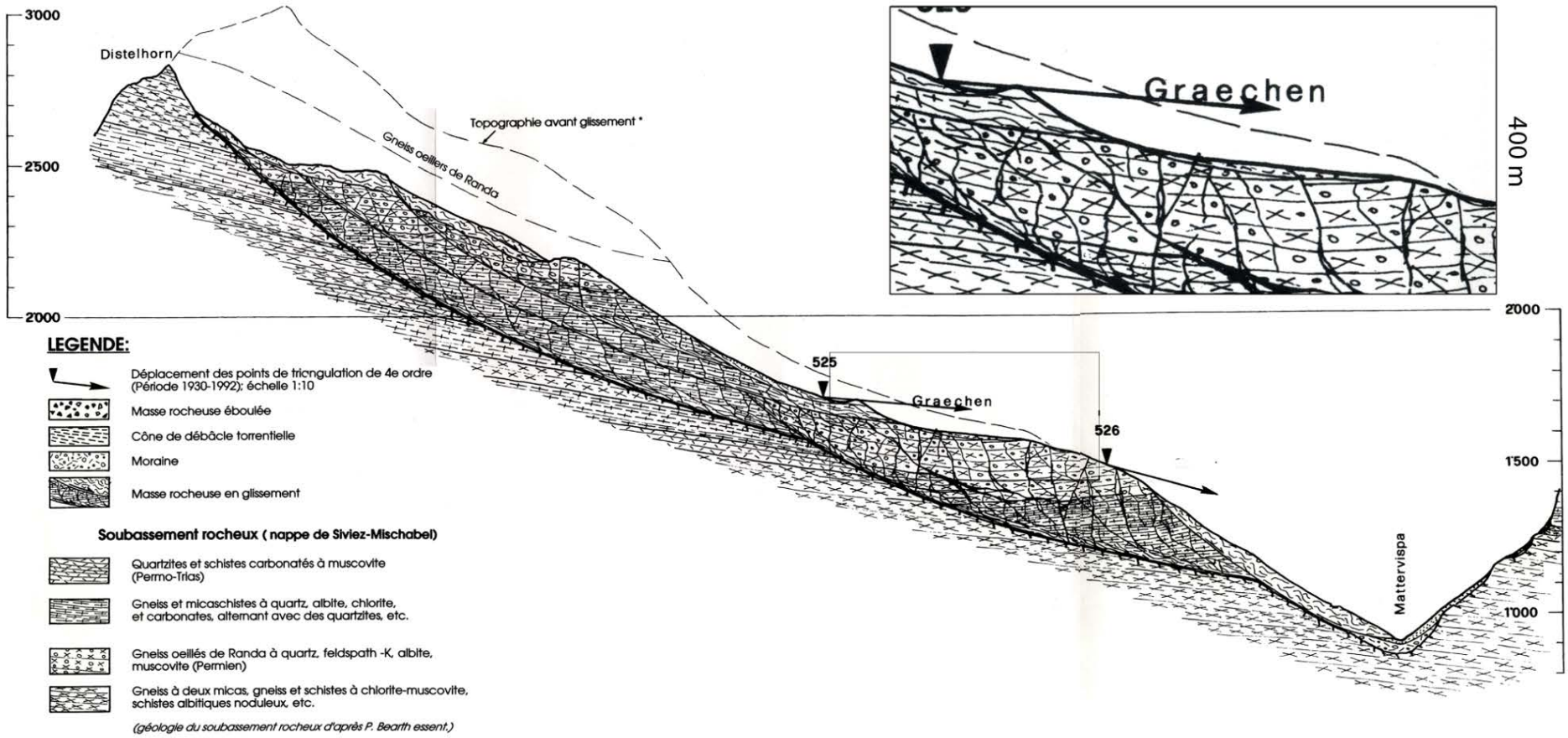

Figure 2 Cross section of the Grächen landslide (Geological atlas)

2 Geo-mechanical models

The studied area is relatively well-known from a geology point of view, and the propagation characteristics of the rock were studied through analysis of actual seisms propagation. In this chapter, important features such as soil constitutive model selection, hydro-mechanical coupling and boundary conditions are addressed.

2.1 Soil constitutive models

Due to lack of enough geo-mechanical information about Grächen, this 2D simulation is considered as a parametric study in order to evaluate the different traditional factors' importance in a seismic scenario. *PLAXIS* is selected for this objective. This software program is based on finite element method, which integrates pre- and post- processors. It also provides an appropriate soil constitutive laws library and the specific boundaries for dynamic problems. Chang et al. (2010) also realized a dynamic analysis of landslide with Mohr-Coulomb constitutive law using *PLAXIS*. Their results correspond with aerial photographic studies.

The bedrock is considered as elastic material and the soil is selected as Mohr Coulomb material. The bedrock behaves frequently as an elastic material in earthquake modelling, which is also widely considered for soil slope analysis (Vidale and Helmberger 1988; BRGM 2007; van Asch *et al.* 2007). Mohr Coulomb model is merely most popular in both static and dynamic soil modelling with finite elements or with finite difference software from the engineering point of view (Cetin *et al.* 2004; Martino and Scarascia Mugnozza 2005; Chang *et al.* 2010; Singh *et al.* 2010) . Mohr Coulomb model is an elastic perfectly-plastic model. In *PLAXIS*, it involves basic input parameters like Young`s modulus E for soil elasticity, cohesion c and friction angle φ for soil plasticity , and dilatancy angle ϕ are required to define the model and MC criterion (Plaxis-Material 2010).

2.2 Governing equations for poroelastic media

The behaviour of pore fluid in terms of movement and pressurization has a strong influence on the deformation of solid skeleton of the soil or the rock. The formulation of this phenomenon therefore is important to be established for this study. Several choices are available in the literature, corresponding to different assumptions. In general, the soil is considered as a saturated material of two-phase composition in a dynamic analysis. In this section, a generalized Biot formulation for such problem will be described. Then for different requirements of study cases, simplified formulations will be proposed. The three main equations governing the interaction of these two phases, the motion equation, mass equation and the Darcy equation have been shown in Eq.[1], Eq. [3] and Eq.[4] :

The momentum conservation for the soil-fluid mixture is given by:

$$\mathrm{div}\,\boldsymbol{\sigma} + \rho \underline{g} = \rho \underline{\ddot{u}}_s + \rho_f \underline{\ddot{u}}_{rf} \qquad [1]$$

In terms of effective stress, it becomes:

$$\mathrm{div}\,\boldsymbol{\sigma}' - \mathrm{grad}\, p + \rho \underline{g} = \rho \underline{\ddot{u}}_s + \rho_f \underline{\ddot{u}}_{rf} \qquad [2]$$

Where

- $\underline{g}$, gravity acceleration vector

- p , pore water pressure
- $\boldsymbol{\sigma},\boldsymbol{\sigma}'$, total Cauchy stress, effective stress in the combined solid and fluid mix at any instant
- ρ , the density of assembly $\rho=(1-n)\rho_s+n\rho_f$
- n , porosity of the porous medium
- ρ_f , ρ_s, the density of fluid phase and the density of solid phase
- $\underline{u}_s$, displacement of solid phase
- $\underline{u}_{rf}$, relative displacement to the solid phase $u_{rf}=n\left(u_f-u_s\right)$
- The divergence operator is defined as $\left\{\mathrm{div}(\boldsymbol{\sigma})\right\}_i=\sum_j \partial_j \sigma_{ij}$
- The gradient operator is defined as $\left\{\mathrm{grad}(p)\right\}_i=\partial_i p$

The mass conservation for a saturated two-phase medium is written in the Eq.[3]

$$\mathrm{div}\,\dot{\underline{u}}_{rf}+\mathrm{div}\,\dot{\underline{u}}_s=-\partial_t p/Q \qquad [3]$$

Where the compressibility variable Q is defined as $\frac{1}{Q}=\frac{n}{K_f}+\frac{1-n}{K_s}$ in which K_s and K_f are respectively the compressibility of solid and fluid phase.

A generalized Darcy law governs the movement of one phase with respect to the other:

$$\dot{\underline{u}}_{rf}=\mathbf{K}\left[-\mathrm{grad}\,p+\rho_f(\underline{g}-\ddot{\underline{u}}_s-\ddot{\underline{u}}_{rf}/n)\right] \qquad [4]$$

where $\mathbf{K}$ is a tensor of permeability which is defined as $\mathbf{K}=k_i/\rho_f g$ in three principle directions (x,y,z). Usually, the permeability in the soil is considered the same in three directions $\left(k_x=k_y=k_z\right)$.

The Eq.[4] then can be putted into Eq.[3], we obtained:

$$\mathrm{div}\,\dot{\underline{u}}_s+\mathrm{div}\left\{\mathbf{K}\left[-\mathrm{grad}\,p+\rho_f(\underline{g}-\ddot{\underline{u}}_s-\ddot{\underline{u}}_{rf}/n)\right]\right\}=-\partial_t p/Q \qquad [5]$$

The flow of pore-fluid for low permeability values is governed by seepage rather than inertial effects (Benzenati and Modaressi 1994). In addition, the acceleration of solid skeleton is much higher than that of fluid phase which therefore can be neglected in the Darcy relationship (i.e. $\ddot{\underline{u}}_{rf}$ is eliminated in Eq.[4]). This formulation called first simplified model 'FSM' or u_s-u_{rf}-p formulation:

$$\mathrm{FSM}\begin{cases}\mathrm{div}\,\boldsymbol{\sigma}'-\mathrm{grad}\,p+\rho\underline{g}=\rho\ddot{\underline{u}}_s+\rho_f\ddot{\underline{u}}_{rf}\\ \mathrm{div}\,\dot{\underline{u}}_s+\mathrm{div}\left\{\mathbf{K}\left[-\mathrm{grad}\,p+\rho_f(\underline{g}-\ddot{\underline{u}}_s)\right]\right\}=-\partial_t p/Q\end{cases} \qquad [6]$$

This formulation is interesting for the loading with a high frequency, for example a frequency above 30Hz (Zienkiewicz and Shiomi 1984; Modaressi 2003; De Martin *et al.* 2007). In the earthquake engineering, the frequency for the loading is not as high as that for the first simplified model. A

suitable range of frequency can reduce the cost for calculation. So the second simplified model ‘SSM’ was considered to be formulated. In this model, in addition to the FSM, the relative fluid acceleration is neglected in Darcy law so that the fluid displacement can be assumed to be eliminated in the momentum equation (i.e. $\underline{\ddot{u}}_{rf}$ is eliminated in Eq.[1] and Eq.[2]). In such case, the unknown variables are the solid displacement and pore water pressure. This model is more popular to be called *u-p* formulation:

$$\text{SSM}\begin{cases}\operatorname{div}\boldsymbol{\sigma}'-\operatorname{grad}p+\rho g=\rho\underline{\ddot{u}}_s\\ \operatorname{div}\underline{\dot{u}}_s+\operatorname{div}\left\{\mathbf{K}\left[-\operatorname{grad}p+\rho_f(\underline{g}-\underline{\ddot{u}}_s)\right]\right\}=-\partial_t p/Q\end{cases} \quad [7]$$

In some special cases, based on the SSM, the acceleration of solid in the Darcy law is possible to be neglected. This is also the basic Darcy law. As a result, the third simplified formulation ‘TSM’ (u-Biot formulation) can be obtained:

$$\text{TSM}\begin{cases}\operatorname{div}\boldsymbol{\sigma}'-\operatorname{grad}p+\rho\underline{g}=\rho\underline{\ddot{u}}_s\\ \operatorname{div}\underline{\dot{u}}_s+\operatorname{div}\left\{\mathbf{K}\left[-\operatorname{grad}p+\rho_f\underline{g}\right]\right\}=-\partial_t p/Q\end{cases} \quad [8]$$

2.2.1 Application domains

In the previous section, the main governing equations are described. However, the application domains are only talked about ambiguously in terms of the level of frequency. In this section, their own domains of application are addressed quantitatively for three simplified formulations. In fact, the coupling problem depends on several aspects such as frequency of solicitation, soil depth and characteristics of soil. For example, if the loading with a low frequency reacts on a deep soil, the influence of fluid cannot be neglected in terms of acceleration. (Modaressi 2003) and (Zienkiewicz and Shiomi 1984) in their works introduced two parameters to define whether or not the coupling problem needs to be taken into account in the study for one-dimensional soil column:

$$\Pi_1=K\rho c_p^2/\omega L^2\ ;\ \Pi_2=\omega L/c_p$$

in which, c_p is the p-wave velocity in the soil and ω is the angular frequency of applied loading.

With these two dimensionless quantities, Figure 3 shows the domain of application:

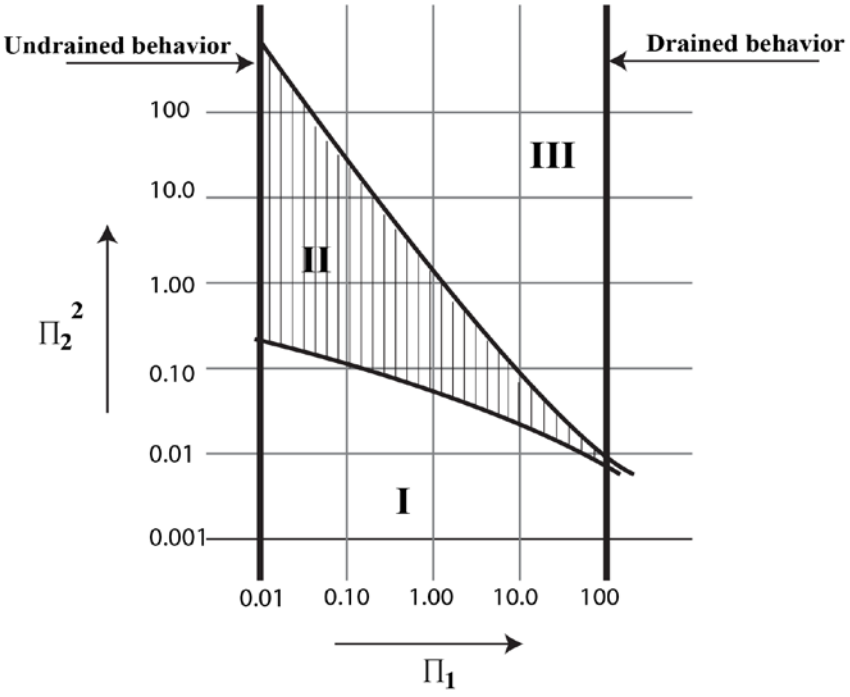

Figure 3 Domain of application for three models (reproduced from (Modaressi 2003))

Zone I : $\ddot{\mathbf{u}}_s, \ddot{\mathbf{u}}_{rf}$ can be neglected 'TSM'

Zone II : $\ddot{\mathbf{u}}_{rf}$ can be neglected 'SSM'

Zone III : none of these terms can be neglected 'FSM'

To calculate two parameters, the main frequency is chosen as 5Hz for an earthquake input. The p-wave in soil stratum of Grächen is in the range of 500 m/s (Burjanek 2010). The permeability of soil is assumed as 10e-4 m/s. An average depth of 40m is chosen for the calculation. After calculation, the result shows the model of Grächen is in the Zone I. A basic Darcy law is adapted to the modelling for Grächen, in addition, the calculated result shows this site can be assumed in a totally undrained behaviour domain.

2.3 Excess pore water pressure

As discussed in previous section, the hydro-mechanical coupling for Grächen is considered as undrained behaviour. In this case, the water cannot dissipate anymore in the soil. The way to define the excess pore water pressure then should be established. According to Terzaghi's theory, principal total stresses in a soil body σ_{ii} can be written in the form of effective stress $\sigma'$and isotropic pore water pressure *p*, as shown in Eq.[9]:

$$\boldsymbol{\sigma}_{ii} = \boldsymbol{\sigma}' + p \qquad [9]$$

where compression is negative for each component, including *p* (Plaxis sign convention).

In *PLAXIS*, pore water pressure is distinguished as steady water pressure and excess pore water pressure.

$$p = p_{steady} + p_{excess} \qquad [10]$$

The steady water pressure is generated by the input of phreatic levels. Excess pore water pressure is generated in the case of undrained material condition.

Water is assumed as a very slightly compressible material in the model. When the soil is set as undrained material, the water doesn't have the time to dissipate in the soil during a very short solicitation. The excess pore water pressure will increase if such a case occurs. In a worst situation, liquefaction could occur in the zone where there is a high concentration of excess pore water pressure. However, the effect of liquefaction is not taken into account in *PLAXIS* (Plaxis-Reference 2010).

The theoretical conception of excess pore water pressure in *PLAXIS* is using Skempton B-parameter. When the soil is set as undrained, *PLAXIS* will automatically determine a new parameter K_u, an implicit undrained bulk modulus, for the whole soil (skeleton soil and water). It distinguishes the total stress, the effective stress and the excess pore water pressure as shown in the following three equations, respectively:

$$\Delta\boldsymbol{\sigma} = K_u \Delta\boldsymbol{\varepsilon} \quad [11]$$

$$\Delta\boldsymbol{\sigma}' = (1-B)\Delta\boldsymbol{\sigma} \quad [12]$$

$$\Delta p = BK_u \Delta\varepsilon_v \quad [13]$$

Where B is the Skempton B-parameter whose value is between 0 and 1

The undrained moduli are automatically calculated by *PLAXIS* using Hook's law of elasticity as shown in the following equations:

$$K_u = \frac{2G(1+\nu_u)}{3(1-2\nu_u)} \quad [14]$$

Where $G = \frac{E}{2(1+\nu)}$; $\nu_u = \frac{3\nu + B(1-2\nu)}{3-B(1-2\nu)}$

2.4 Absorbent boundary

In *PLAXIS* an absorbent boundary is available, with a different formulation from the paraxial elements seen in Del. 3b.3.4 and 3b.3.6. It is named absorbent boundary, and uses a viscous dashpot (damping) analogy. It is simpler in terms of formulation than paraxial elements. However, the simple formulation results in some limitations. The principles are described below.

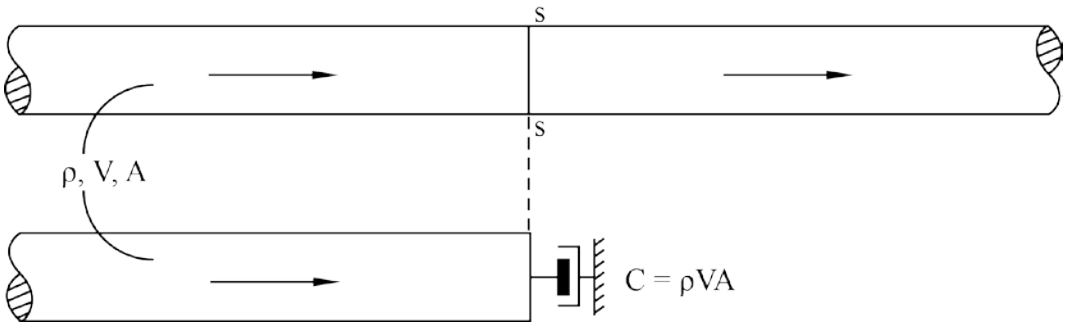

Figure 4 Mechanism of the absorbent boundary in PLAXIS. (ρ mass density of material; V wave velocity; A area of cross section s-s)

Assuming that wave propagates in an infinitely long medium, for example a one-dimensional beam in the Figure 4, the total force induced by the wave on cross-section s-s is:

$$F_s = A \cdot \sigma_s = C \cdot \dot{u} = \left(\rho \cdot V \cdot A \right) \cdot \dot{u}$$

Here A is the area of cross-section $s-s$, V is the velocity of incident wave and ρ is the density of the medium

Hence, as shown in Figure 4, one could replace the semi-infinite portion of the beam to the right of $s-s$ by a viscous dashpot of a constant coefficient in terms of the stress (A is a unit area, i.e., A=1):

$$C = \rho \cdot V$$

Because the dashpot fully absorbs the energy or the stress of incident waves, the motion to the left of s-s will not be affected.

Based on the above conception, relaxation coefficients have been introduced in *PLAXIS* (Plaxis-Dynamic 2010) to improve the effects of absorption. The following equations are written in terms of normal stress and shear stress:

$$\sigma_n = C_1 \cdot C \cdot \dot{u} = C_1 \cdot \rho \cdot V_p \cdot \dot{u}$$

$$\tau = C_2 \cdot C \cdot \dot{u} = C_2 \cdot \rho \cdot V_s \cdot \dot{u}$$

Here, C_1 and C_2 are the relaxation coefficients whose range varies from 0 to 1. When only a pressure wave strikes perpendicularly the boundary, no relaxation will occur $C_1 = 1$. V_p and V_s are the pressure wave velocity and the shear wave velocity, respectively.

From experience gained, $C_1 = 1$ and $C_2 = 0.25$ are reasonable values for absorption of waves at the boundary (Plaxis-Dynamic 2010). It should be noted that due to the limitations of absorbent boundary in *PLAXIS*, a combination of shear wave and pressure wave is however not possible to be fully absorbed. Hence, a boundary effect is still visible in such a case.

A simple analysis involving wave propagation in a one-dimensional medium is presented in the following in order to evaluate effects of the absorbent boundary. The one-dimensional soil column is 20 meters high and 4 meters wide with standard fixities as shown in Figure 5. A mesh with 15-nodes elements is generated. The analysis includes the pure pressure wave propagation and pure shear wave propagation.

A prescribed vertical or horizontal displacement of one centimetre is applied at the bottom of the soil column, which creates a pressure wave or a shear wave, respectively. The soil column is assumed as an elastic medium with a wave velocity V_p equal to 100 m/s and V_s equal to 50 m/s. Therefore, it costs 0.1s for the pressure wave to arrive at the middle of the soil column and 0.2s to reach the top of the column. The case of shear wave propagation costs a double time.

In the case of pure pressure wave, the shear absorbent parameter C_2 is not relevant. The value of C_1 is set as 1, i.e., the boundary will, theoretically, totally absorbs the input wave.

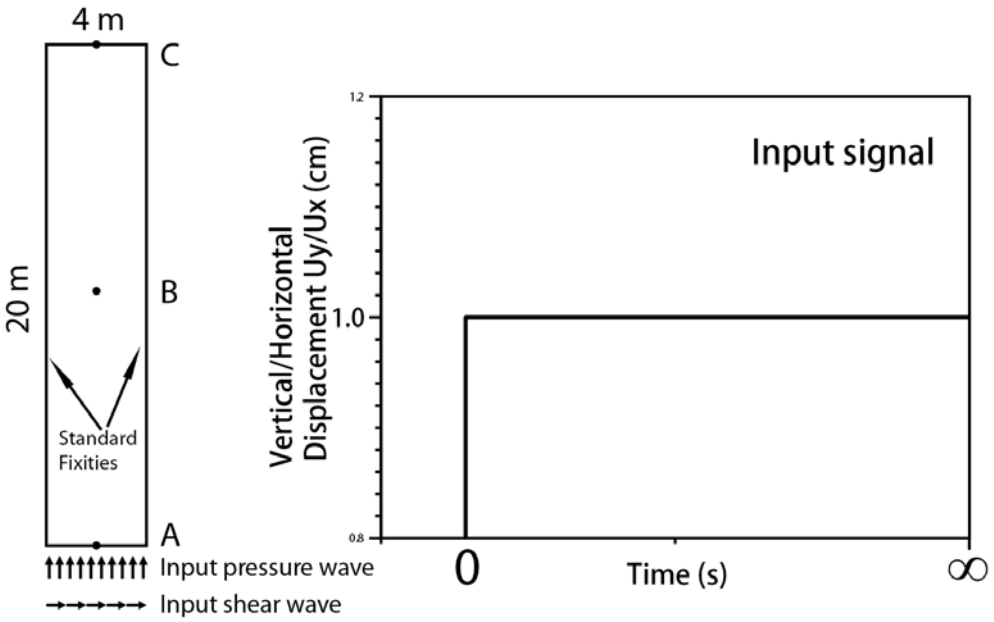

Figure 5 Test model with one dimensional soil column and time-displacement curve of input wave

Two different conditions on the top will be discussed: a) free boundary; b) absorbent boundary. Figure 6 to Figure 9 show the responses of these two different conditions, respectively. The results are saved at the bottom, Point A, in the middle, Point B and on the top, Point C.

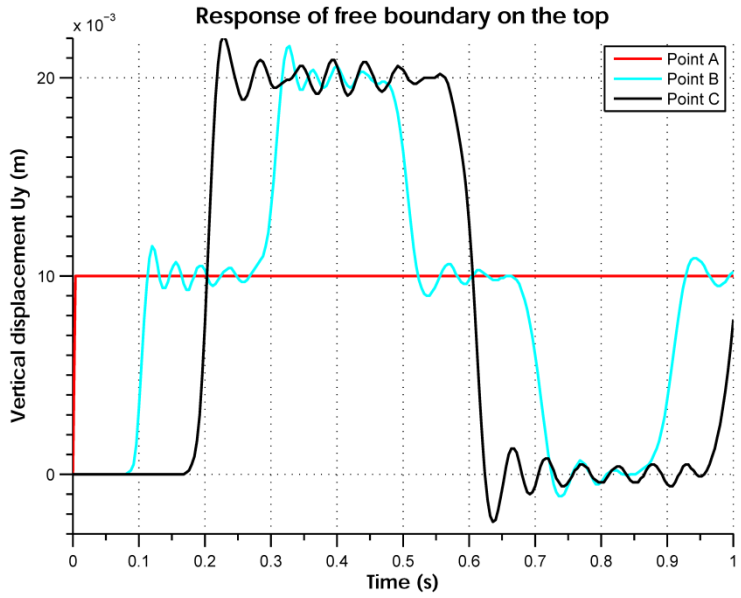

Figure 6 Time-displacement curve with incident pressure wave, free boundary on top of the column

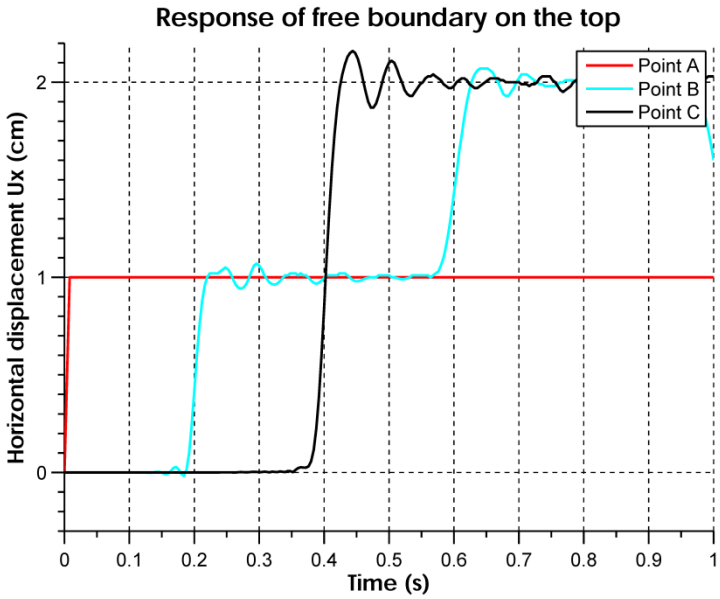

Figure 7 Time-displacement curve with incident shear wave, free boundary on top of the column

As shown in Figure 6 (the same observation in Figure 7), the well-known response of a sample with free boundary on top to such loading is verified. After 0.1 second from the beginning, the wave arrives at the point B. The displacement at point B is more or less equal to 1 cm. Due to the non-analytic nature of the calculation, numerical oscillations are observed, but in general, the displacement is similar to the input and can be recognized as the analytical response.

From the classical theory of wave propagation in the elastic medium, if the propagating wave ends by a free boundary, the reflected wave will double the displacement. In addition to free boundary, the displacement is cancelled by reflected wave to a fix boundary. Hence, at 0.2 second, the wave reaches the top, the displacement recorded at point C is 2 times bigger than that of input displacement, which is exactly due to the effect of free boundary. As soon as arriving at the point C, the wave is reflected and propagates downwards. Therefore, the reflected wave arrives at point B again at 0.3 second and enhances the displacement of point B to 2 cm. This reflected wave propagates until reflected by the fixed boundary at the bottom and attenuates the displacement at the point B at 0.5 second. 0.1 second after, it attenuates the displacement at the point C. Event times correctly differ in Figure 7 due to p-wave and s-wave velocities being different.

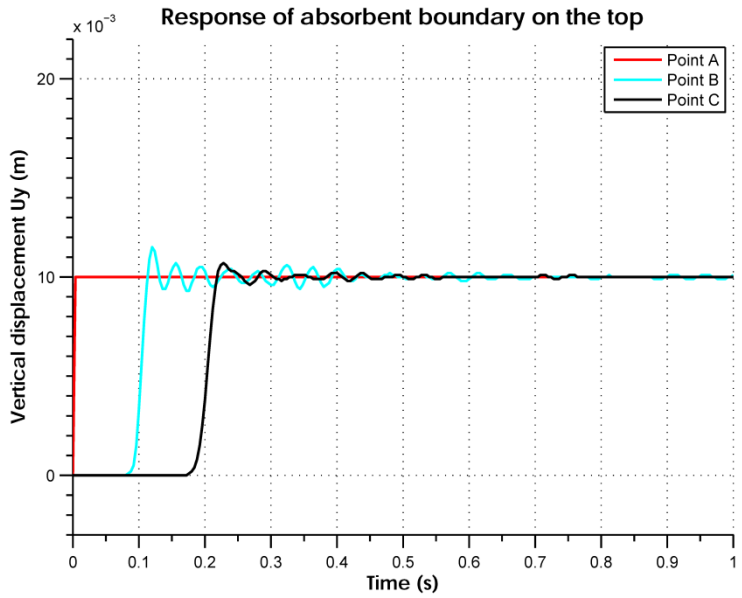

Figure 8 Time-displacement curve with incident pressure wave, absorbent boundary on the top of soil column

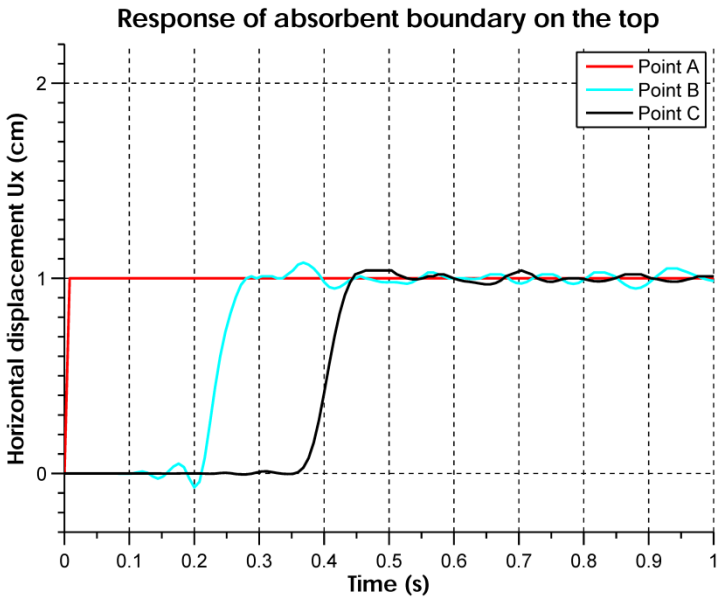

Figure 9 Time-displacement curve with incident shear wave, absorbent boundary on the top of soil column

Compared to previous observation, the effect of absorbent boundary is obvious as shown in Figure 8 and Figure 9. The point B and C both move up to 1cm as input signal and became steady with no amplification and attenuation of displacement, which is in contrast to the previous case. The absorbent boundary exhibits the significant effect in preventing the wave reflection that is expected. The same results were observed in the pure shear wave test. As a conclusion, the results showed a good agreement with the theory. However due to the numerical precision of the finite element method, there are some perturbations in the response. But it is sufficient for practical approach and sensitivity analysis.

3 Two-dimensional sensitivity study for Grächen

Following paragraphs present the synthesis of sensitivity study which concerns hydraulic condition variations such as the level of water table and mechanic properties of soil for example: elastic modulus, cohesion and friction angle.

3.1 Finite element model

Geometry is realized by the interpretation of several geological cross sections and aerial photos. General dimension is mentioned in the Figure 10. Section of slope part is about 3600m^2 with a length of 600m and a max depth of 60m. Slope part with an angle about 10 degree represents the village of Grächen, which is the main interesting zone.

The zone of interest (location of the village) is relatively small compared to the whole geological cross section. The model nevertheless extends to a large scale. Restrictions in the way dynamic displacements can be entered as input and in the way absorbent boundaries can be placed led to this choice. The mesh is generated with 15-node elements. The number of elements is 591 of which 112 are for soil layer. The mesh along the interface between bedrock and soil is refined. The effect of a seism on the deep-seated rock movement is not considered here.

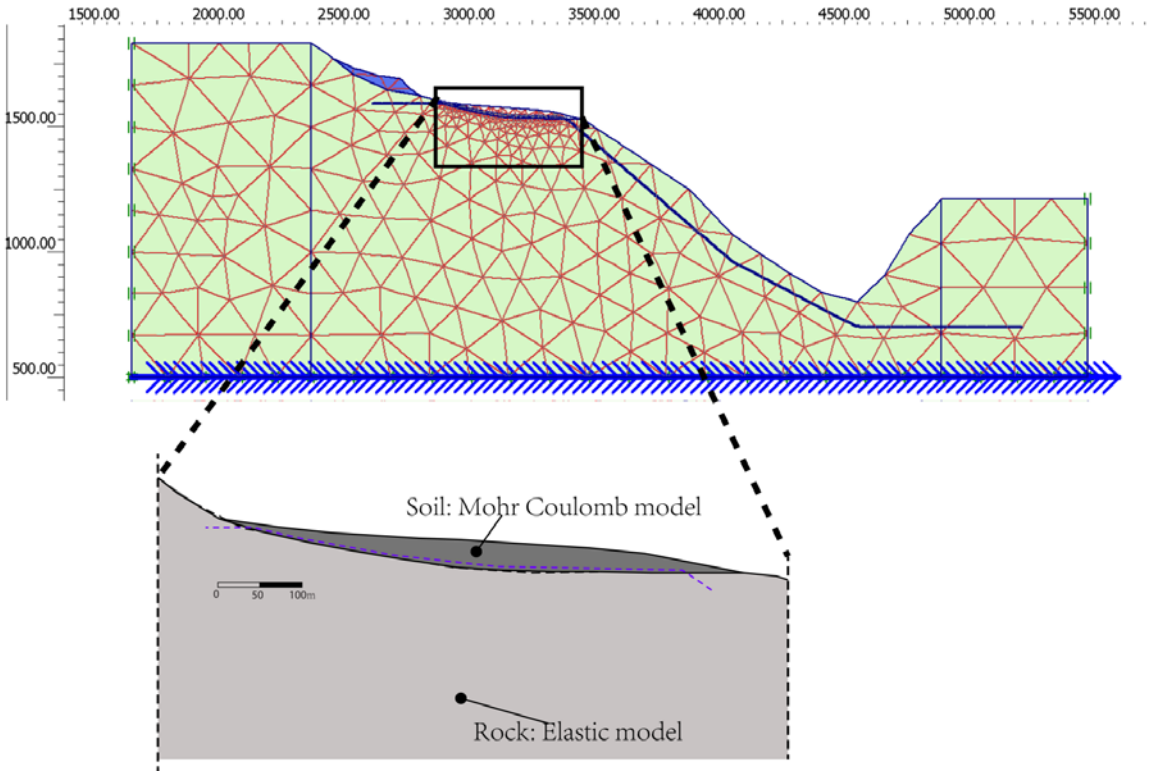

Figure 10 Mesh and geometry

In order to avoid the reflection problem at boundary in analysis, a couple of vertical absorbent boundary is set at the left and right hand of model in order to absorb waves arriving at the boundary.

Due to the prescribed displacement at the bottom, no absorbent boundary can be used, as the absorbent boundary requires displacement freedom. Therefore the absorbent boundary cannot be used at the bottom. So the bottom is positioned “far away” from the study slope.

And also standard fixities are added at both sides and the bottom of the model. During the static analysis, for example, at stage construction, weight activation and plastic analysis, the standard fixities will be activated.

As soon as dynamic stage starts, the absorbent elements will be switched on and meanwhile the standard fixities will be off. At the same time, the nodes at bottom will be fixed in the vertical direction and freed in the horizontal direction in order to apply the seismic input motion.

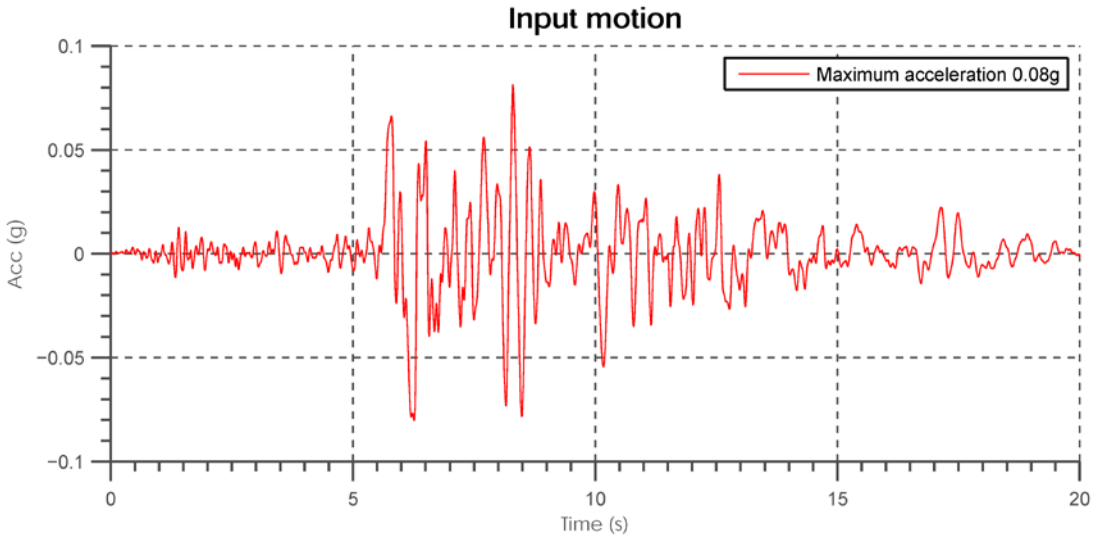

Figure 11 Input Horizontal Accelerogram from USGS.

Figure 11 shows the acceleration time history extracted from United States Geological Survey. Its moment magnitude is 6.5. It is an accelerogram recorded of earthquake whose epicentre is 65km far away and it produces peak acceleration equal to 0.08g. The first significant variation of amplitude of acceleration occurs about 6.5 second after the beginning of the earthquake.

3.2 Material properties

This analysis involves a study of the influence of basic input parameters like Young`s modulus E for soil elasticity, cohesion c and friction angle φ for soil plasticity. The variation of these parameters was realised only in the soil stratum. The selected range of Young's modulus is from 50MPa to 2GPa, cohesion is from 20kPa to 50kPa and friction angle is from 20° to 50°. These values cover a wide spectrum and the goal is mainly to investigate the sensibility of the results to their variations rather than to predict displacement with as-yet-unmeasured actual soil characteristics in Grächen. As can be seen in Section 2.2, the permeability doesn't play a role in the calculation under undrained condition.

When using Mohr-Coulomb and linear elastic models, the wave velocities V_s and V_p are calculated from the elastic parameters and soil density (Plaxis-Dynamic 2010).

Rock (Elastic material)	Mass density	20	kN/m3
	Young Modulus	30	GPa
	Poisson ratio	0.3	-
Soil cover (Mohr Coulomb material)	Mass density	17	kN/m3
	Young Modulus	50, 200, 2000	MPa

	Poisson ratio	0.3	-
	Cohesion	20,25,30,35,40,45,50	kPa
	Friction angle	20,25,30,35,40,45,50	°

Table 1 Summarization of material information

3.3 Sensitivity analysis

The initial conditions are presented first. Figure 12 shows the recorded points and the selected cross section. The initial vertical effective stress distribution and shear stress distribution are presented in Figure 13. It can be observed that a region of maximum shear stress is located at the bottom of slope, which could induce failure when excess pore water pressure builds up in this region.

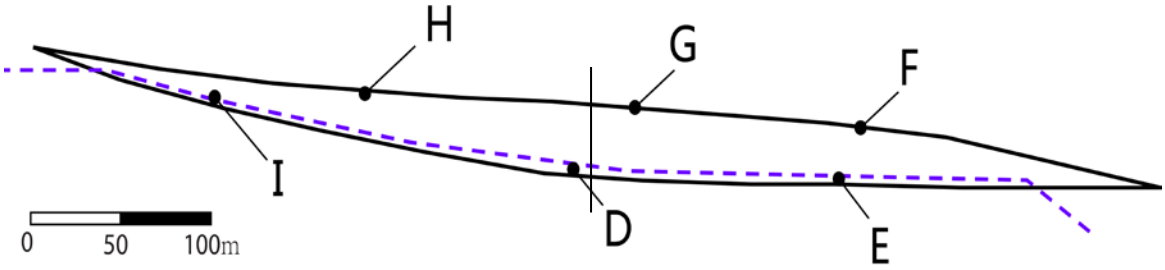

Figure 12 Recorded points and cross-section

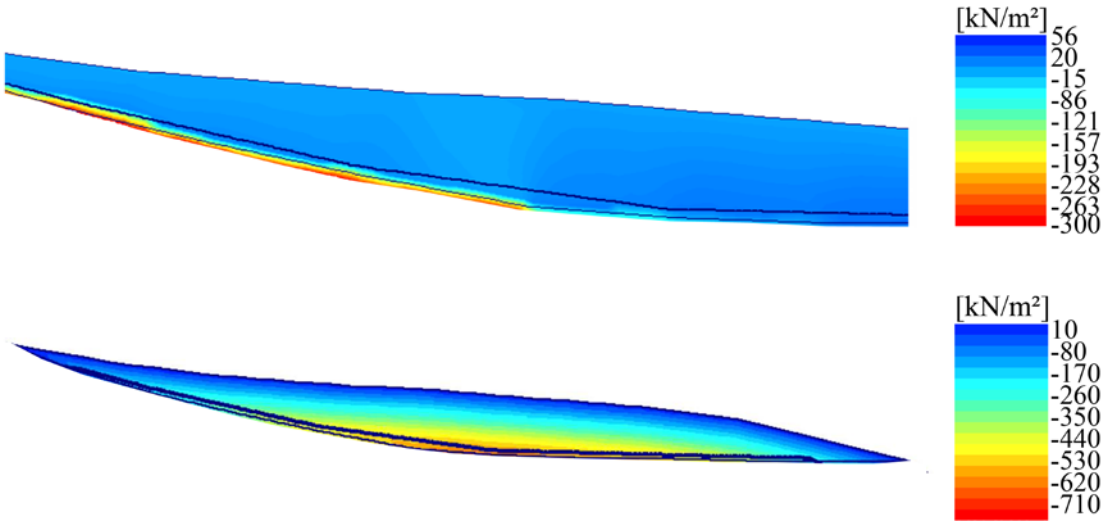

Figure 13 Above: initial shear stress, Below: initial vertical effective stress

3.3.1 Displacements

Figure 14 shows the observed final displacements at three locations at the surface of the model as a function of soil Young's modulus. As can be observed, the displacement at the uphill of slope (point H) is always bigger than the lower parts of slope. A decrease of elastic modulus induced an increase of displacement, which is almost linear in a logarithmic scale.

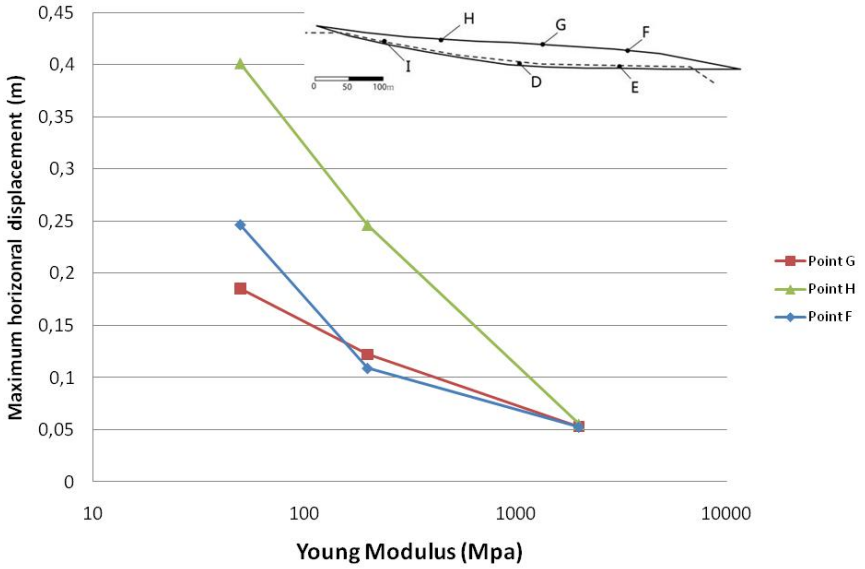

Figure 14 Evaluation of young modulus (c=40kPa and ϕ=30°) at three points in logarithmic scale.

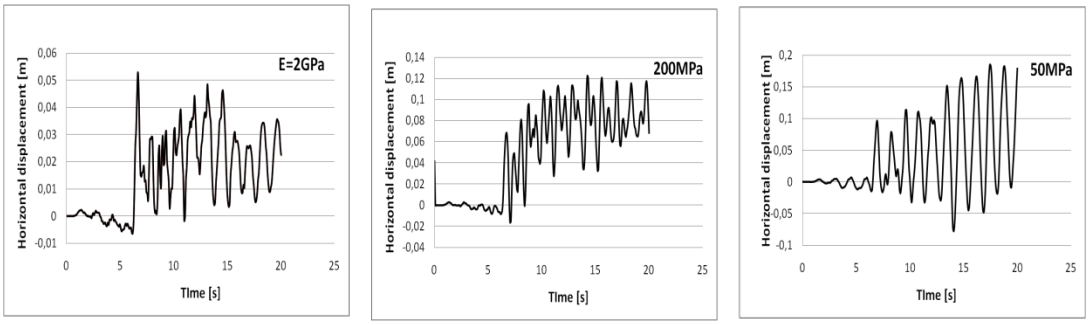

Figure 15 Horizontal displacements with three values of Young Modulus recorded at Point H

In terms of displacement response at surface, the results are shown in Figure 15. The observation of peak value is the same as the conclusion in the previous paragraph. However, when regarding the form of response, one can find when E=50MPa, a mono frequency shows in the response 10s after the beginning of earthquake.

A possible explanation to this observation is the resonance of soil. We attempted to show the possibility of this phenomenon. Due to the complexity of geometry, we regard the soil below the Point H as one dimensional soil column. The first natural frequency of one dimensional soil column is

$$f_1 = V/4H \qquad [15]$$

Where, V is the wave velocity and H is the height of the soil stratum.
When E=50MPa, the shear velocity is equal to about 105 m/s. The depth of soil below the point H is equal to about 33m. Therefore, the first natural frequency is about 0.79Hz. The range of uncertainty is ±0.1 Hz.

The Fast Fourier transform of the first 10s of the input accelerogram is shown in the Figure 16.

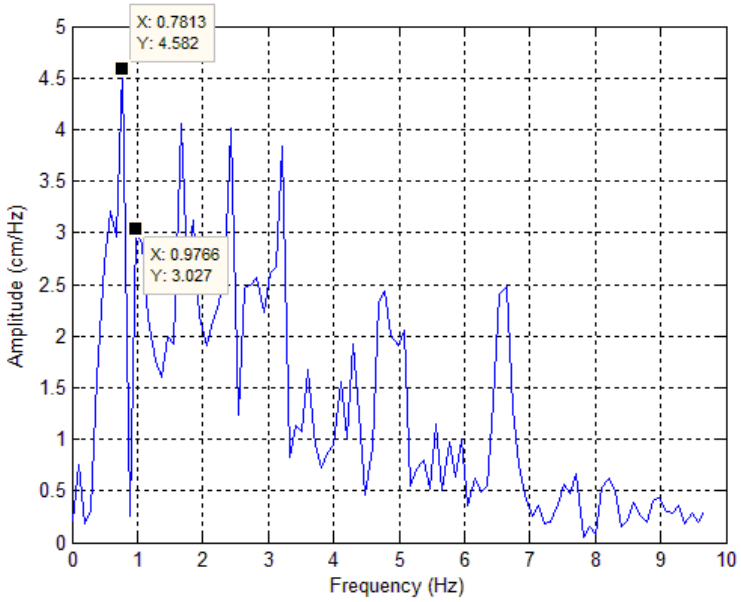

Figure 16 Fast Fourier response of input motion from 10s after the beginning of the earthquake

We can see from the response, the first peak occurs at 0.78Hz. This is almost the same value as the soil column natural frequency. The possible resonance may occur at this zone. But from the study of COGEAR, the shear velocity would not be lower than 105m/s. So actual resonance of soil would be an unlikely case for the site of Grächen.

3.3.2 Excess pore pressure

Figure 17 shows a comparison of excess pore pressure creation at three locations (one per row) and with various plastic parameters. Various cohesions are shown in the left column and various friction angles in the right column. As can be observed from the results in Figure 17, the pore water pressure increases at about 7.5 second after the beginning of earthquake (compressive stresses, including pressures, are negative in *PLAXIS*). It is about 1 second later than the moment that the first important variation of input acceleration occurred.

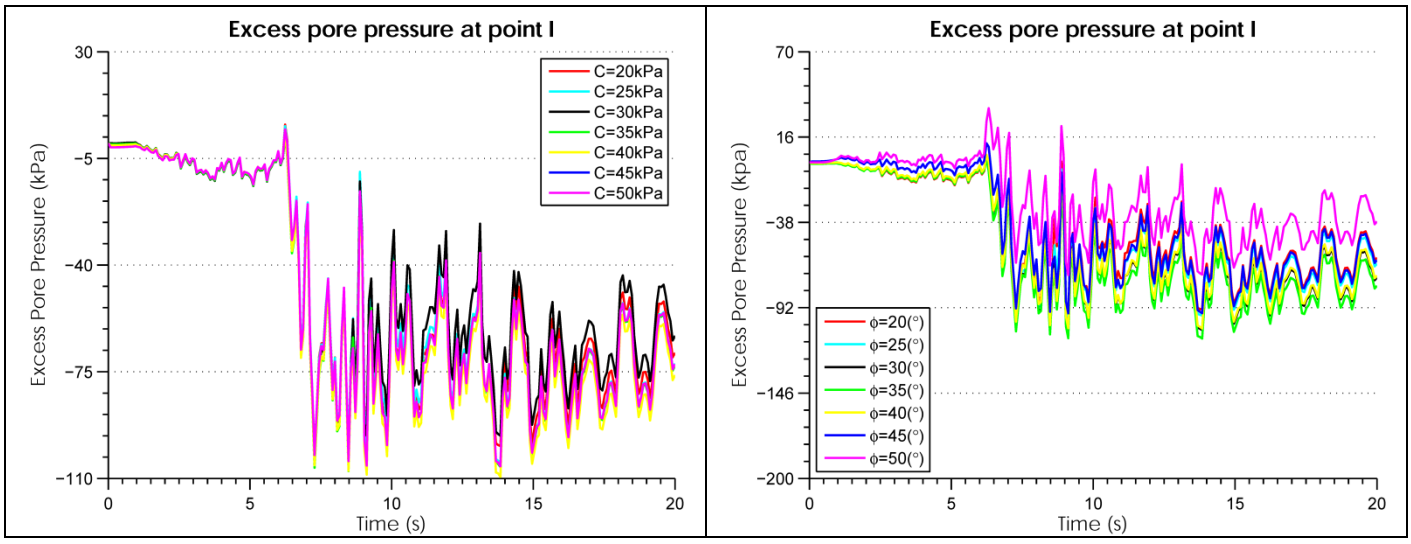

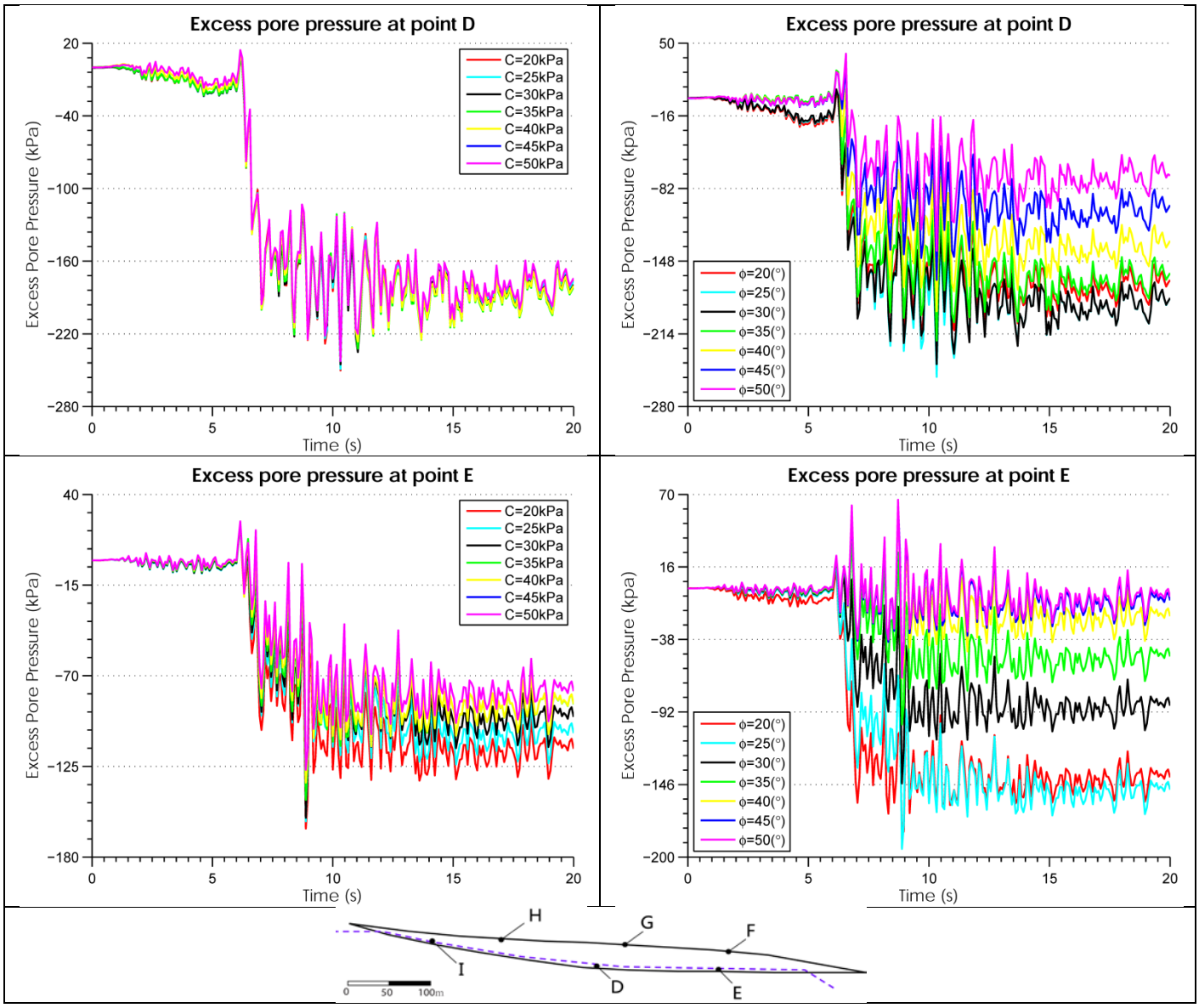

Figure 17 Time - excess pore water pressure curve with constant ϕ = 30° (left) and C = 35kPa (right)

The stress state will reach the failure limit more quickly if the yield limit is lower (lower cohesion or lower friction angle). After, more volumetric plastic strain will occur. From the theory of excess pore water pressure of *PLAXIS*, the excess pressure is proportional to the volumetric strain. Therefore, the lower the yield surface is, the more excess pore water pressure is generated. This is found to be the case in these graphs.

From this group of figures, we can observe that at point E, the influence of friction angle is more significant than that of the cohesion. At Point I, even the water table just located above the point, the pore pressure initial is low. However, the increase of excess pore water pressure is significant, up to 100 kPa.

The constitutive law used here does not allow the excess pore water pressure to dissipate. As shown in figure, the excess pore water pressure remains a high value at the end of the earthquake.

3.3.3 Amplification ratio

Figure 18 shows the evolution of the ratio between peak ground acceleration and peak input acceleration (called amplification ratio) with variations of plastic parameters. Due to the topography of site, the three selected zones have very different behaviours. It should first be noted that in comparison with the results obtained on a soil column, a significant increase in the amplification ratio is found. This trend is not dependant on soil parameters and as such should be interpreted as a strong effect of local topography.

In the high part of the slope, Point H, the amplification ratio is increasing linearly with the cohesion and friction angle at the whole range. Point G is located at the middle of the soil area. It still has a relatively large amplified vibration, which results from the focusing of waves due to topography. This site is then considered as an unfavourable site. Quantitatively, the amplification ratio is close to be proportional to the cohesion and friction angle at a range smaller than 30kPa. After 30kPa, there is nearly no effect of cohesion and friction angle on the response of this point. The amplification is up to 6.4 in maximum.

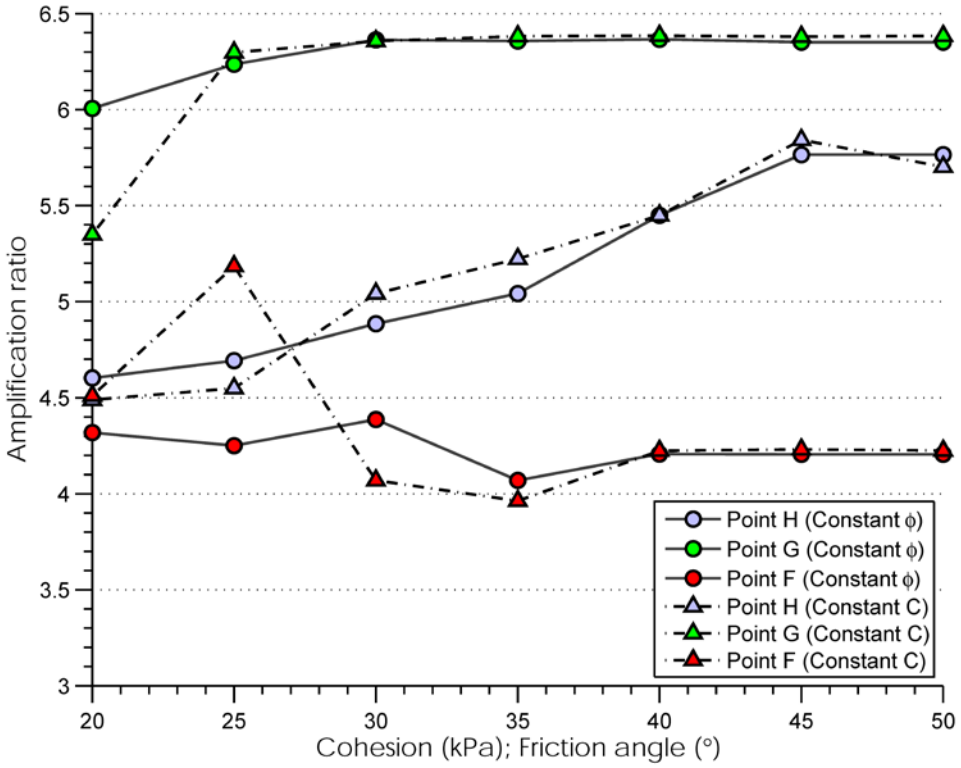

Figure 18 Amplification ratio between peak ground acceleration and peak input acceleration in the horizontal direction of 3 points at surface of the area. Constant ϕ = 30° and Constant C= 35 kPa

Point F is below and to the right of Point G. Amplification ratios all located between 4 and 4.5, and it seems that the cohesion has no significant influence on peak ground acceleration. No trend can be identified relating friction angle and amplification ratio.

Compared to the observation of one dimensional simulation, the amplification ratio is much higher in the two dimensional simulation. In one dimensional simulation, *CyberQuake* considers soil column is infinitive along the horizontal direction, which avoids reflections due to the vertical boundaries. Also the soil material is assumed with a cyclic non-linear behaviour. Due to this assumption, energy is dissipated during each cycle, while in this simulation displacement higher than the previous maximum are needed to dissipate energy. In addition, the base of soil column is deformable and absorbent in the

one dimensional studies, which allows reflected waves to be dissipated at boundaries. However, the model in the two dimensional simulation is on an elastic rigid base that has not the capacity to absorb reflected waves. As shown in Figure 19, the topography makes the input wave reflect in a random way in soil body, which could be an important reason for the higher observed amplification ratios.

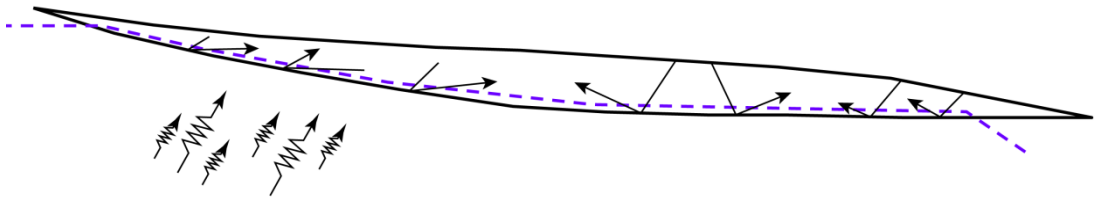

Figure 19 Illustration of wave reflections in soil body

3.3.4 Ru ratio

The Ru ratio is defined as the ratio between the excess pore water pressure Δp and effective vertical stress σ_v', $Ru = \Delta p / \sigma_v'$. The excess pore water pressure is more sensitive to the friction angle than the cohesion. As observed in Figure 20, in the case of low friction angle, the excess pore water pressure at Point E is extremely high compared to other points. Figure 20 shows the same observation from another point of view. A Ru ratio of 0.95 is observed at Point E with the loose materials (low friction angle 20-25°), which will reduce the effective stress and could produce liquefaction failure. In addition, this point is located in the lower part of slope, if liquefaction occurs, the failure will induce a sliding plane at the bottom of slope, which could cause the upper part to fall down as a result if the interface friction at the right side of the soil stratum is overcome.

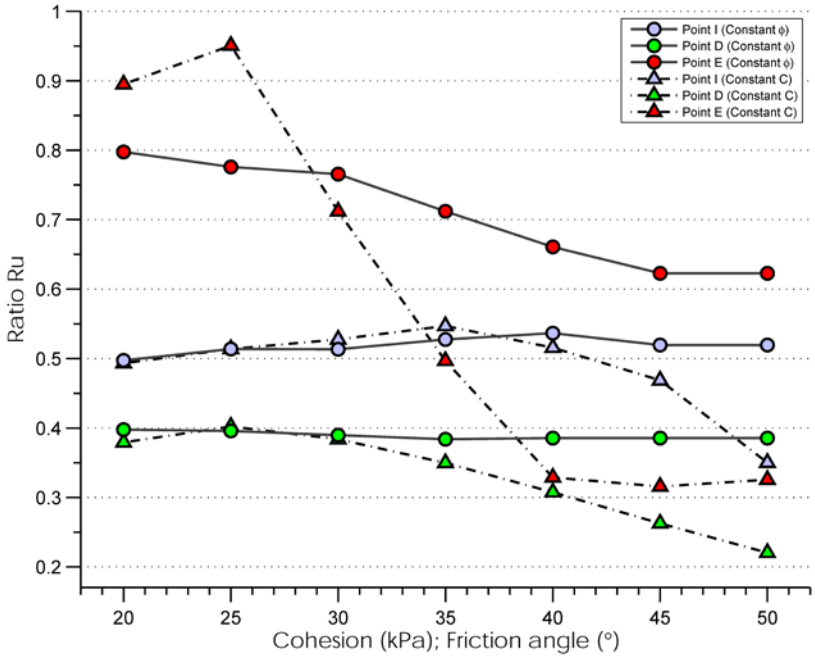

Figure 20 Cohesion/Friction angle – Ru Ratio curve

3.3.5 Water table

Due to lack of information concerning water level variations, an increase of water table level from +0m, +6m to +12m was considered to carry out in the study to improve the interpretation. The

simulation was conducted with selected less favourable friction angle from 20° to 30°. The results are shown in Figure 21. The effect of the increase of the water table level is found to be linear in terms of maximum displacement. At the point F, the influence is minor at the high friction angles.

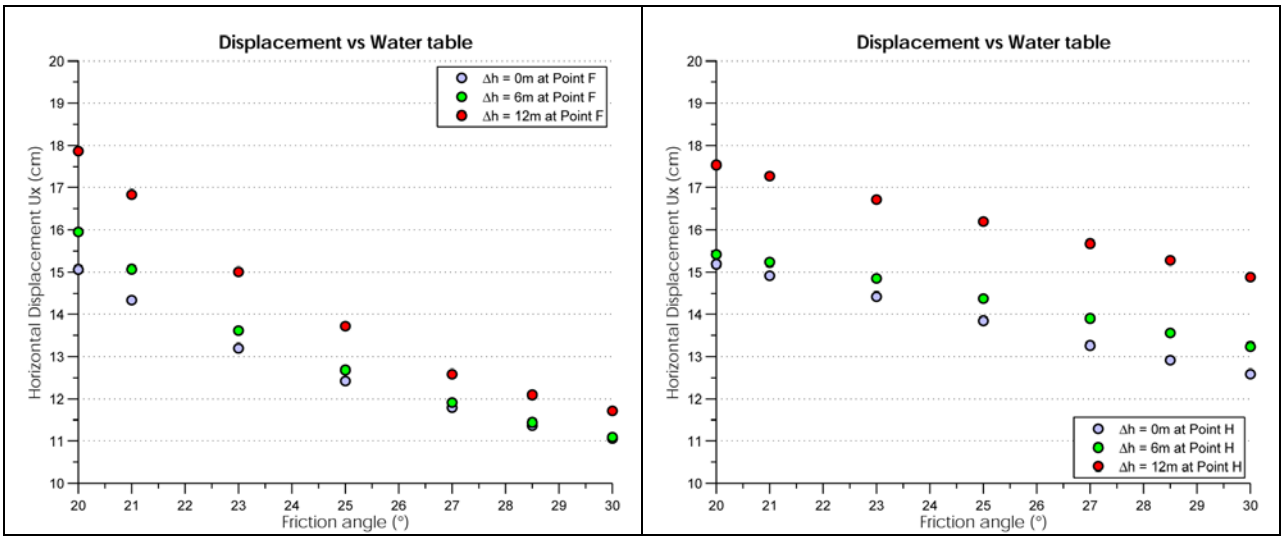

Figure 21 Influence of the level of water table on the maximum horizontal displacement during the dynamic analysis, at points F (left) and H (right).

3.3.6 Cross section representation

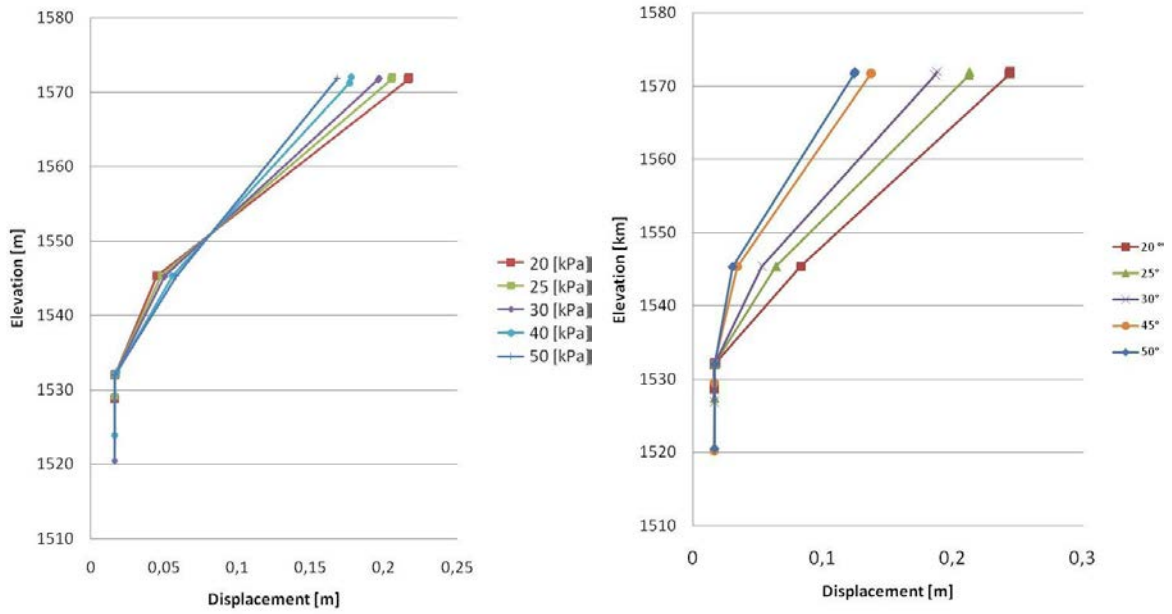

Figure 22: Horizontal displacement at 10 s as a function of depth, (left) for varying cohesions with ϕ = 30°, (right) for varying friction angles at c= 35 kPa.

Figure 22 shows the displacements after 10s after the beginning of earthquake for varying yield surfaces. The influence of cohesion is less significant than the influence of friction angle. This is logical as the depth of the soil layer creates stresses much higher than the maximum tested cohesion, in which case the friction angle has more influence on the plastification stress. A higher cohesion prevents plastic strains in the upper part of soil and therefore concentrates energy dissipation, and displacements, in the lower part. On the right-side figure, it can be seen that friction angle influence is

not only larger, it can be seen throughout the soil. An increase in the friction angle limits the displacements in the lower part of the soil, while the top-part is less affected in this specific geometry.

Conclusion

A parametric study with Mohr-Coulomb model was performed in this study of the Grächen site. It is observed that site effects are important due to complexity of wave propagation in a soil body. Different locations have different levels of amplification, which are mostly related to the geometry rather than to the exact layering in a case of relatively homogeneous wave-speeds. Amplifications up to six times higher than in the case of a soil column (Del. 3b.3.6) were found.

The sensibility of a mountain site seismic case study to geotechnical parameters was investigated. It was found that wave-speeds and friction angle were the most important elements in a geotechnical investigation destined to the evaluation of seismic risk. The first parameters, that are linked with elastic properties, remain crucial in the intensity of the observed displacements. Friction angle affects site response in two ways: directly as a plastic parameter, but also indirectly as it contributes to the development of excess pore pressures in saturated zones by controlling volumetric soil behaviour. The third effect is the water table position, which can modify the site response but in a less visible way. Soil cohesion was found to be less significant of the tested parameters.

More information would have been brought by further field investigation such as undisturbed sampling. Also a more complete constitutive model, calibrated with the samples, and a better knowledge of local hydrology for dynamic analysis should be considered in further studies for this region.

References

Benzenati, I. and Modaressi, H. (1994). Paraxial approximation for poroelastic media. *Soil Dynamics and Earthquake Engineering* **13**(2): 117-129.

BRGM (2007). *Application of numerical models to case histories: Earthquake cases - Phase II*. Risk mitigation for earthquakes and landslides integrated project. LESSLOSS, Deliverable 96b.

Burjánek, J., Gassner-Stamm, G. and Fäh, D. (2010). *Array-measurements in the area of Visp and St. Niklaus*. COGEAR, Del. 3.1.2.

Burjanek, J., Gassner-Stamm, G., and Fäh, D. (2010). Array - measurements in the area of Visp and St. Niklaus.

Cetin, K. O., Isik, N. and Unutmaz, B. (2004). Seismically induced landslide at Degirmendere Nose, Izmit Bay during Kocaeli (Izmit)-Turkey earthquake. *Soil Dynamics and Earthquake Engineering* **24**(3): 189-197.

Chang, K.-T., Wan, S. and Lei, T.-C. (2010). Development of a spatial decision support system for monitoring earthquake-induced landslides based on aerial photographs and the finite element method. *International Journal of Applied Earth Observation and Geoinformation* **12**(6): 448-456.

De Martin, F., Modaressi, H. and Aochi, H. (2007). Coupling of FDM and FEM in seismic wave propagation.

Giardini, D., Wiemer, S., Fäh, D. and Deichmann, N. (2004). *Seismic hazard assessment of Switzerland*, Swiss Seismological Service.

Martino, S. and Scarascia Mugnozza, G. (2005). The role of the seismic trigger in the Calitri landslide (Italy): historical reconstruction and dynamic analysis. *Soil Dynamics and Earthquake Engineering* **25**(12): 933-950.

Modaressi, A. (2003). *Modélisation des milieux poreux sous chargements complexes*. PhD thesis at LMSSMat, Ecole centrale de Paris.

Plaxis-Dynamic (2010). *PLAXIS 2D Dynamic Manual Version 9.0*.

Plaxis-Material (2010). *PLAXIS 2D Material Models Manual Version 9.0*.

Plaxis-Reference (2010). *PLAXIS 2D Reference Manual Version 9.0*.

Singh, T. N., Verma, A. K. and Sarkar, K. (2010). Static and dynamic analysis of a landslide. *Geomatics, Natural Hazards and Risk* **1**(4): 323 - 338.

van Asch, T. W. J., Malet, J.-P., van Beek, L. P. H. and Amitrano, D. (2007). Techniques, issues and advances in numerical modelling of landslide hazard. *Bulletin de la Societe Geologique de France* **178**(2): 65-88.

Vidale, J. E. and Helmberger, D. V. (1988). Elastic finite-difference modeling of the 1971 San Fernando, California earthquake. *Bulletin of the Seismological Society of America* **78**(1): 19.

Zienkiewicz, O. C. and Shiomi, T. (1984). Dynamic behaviour of saturated porous media; The generalized Biot formulation and its numerical solution. *International Journal for Numerical and Analytical Methods in Geomechanics* **8**(1): 71-96.